JMEPEG (2018) 27:4855–4870
https://doi.org/10.1007/s11665-018-3591-4

1059-9495/$19.00

Mechanism of Decrease in Impact Toughness in a Low-Carbon MnCrMoNiCu Plate Steel with Increasing Austenitizing Temperature

Mi Luo, Dongsheng Liu, Binggui Cheng, Rui Cao, and Jianhong Chen

(Submitted March 2, 2018; in revised form July 2, 2018; published online August 24, 2018)

In order to reveal how microscopic factors affect the toughness and the occurrence of cleavage fracture of a low-carbon MnCrMoNiCu alloyed steel, a series of thermal treatments was performed on the steel employing a thermomechanical simulator. These involved reheating samples at different temperatures (950-1250 °C), producing different prior austenite sizes, followed by a continuous cooling transformation process. The Charpy V-notch toughness was determined, and the effect of austenite grain size on the ductile-to-brittle transition temperatures of the steel was investigated. The microstructural evolution on the austenite sizes was studied, fracture features were characterized, the critical event for cleavage fracture was identified, and the local cleavage fracture stress σ_f was calculated. The impact toughness decreased as the austenitizing temperature increased. A quantitative relationship between σ_f and the size of the initial cleavage fracture facet (microcrack nucleus) a_f in the lathy martensite + bainite microstructure has been developed.

Keywords austenitizing temperature, cleavage fracture stress, impact toughness, mechanism, packet size

1. Introduction

Engineering significance in revealing the cleavage fracture behavior and variation of ductile-to-brittle transition temperature (DBTT) has stimulated substantial research works using the principle of micromechanism of the cleavage fracture in steels (Ref 1-7). The cleavage fracture takes place under the condition that the applied stress at the tip of a preexisting crack exceeds the local critical fracture stress. The local cleavage fracture stress, σ_f, is a function of the surface energy of the fracture, γ_p, and the initial crack size, r, according to the Griffith equation. It is an intrinsic mechanical property of the steel offered by the weakest microstructural component to the propagation of cleavage cracking. Assuming an infinite plate with a penny-shaped crack in length r, the Griffith form of σ_f can be expressed as follows:

$$\sigma_f = \sqrt{\pi E \gamma_p / (1-\nu^2) r}, \quad \text{(Eq 1)}$$

where E is Young's modulus, 200,000 MPa, and ν is Poisson's ratio, 0.3. r can be replaced by the packet size of bainite or martensite d_p (Ref 2, 5), when the critical event of cleavage crack process is the propagation of a small crack originated in a single packet to the adjacent one, i.e.,

$$\sigma_f = \sqrt{\pi E \gamma_p / (1-\nu^2) d_p}. \quad \text{(Eq 2)}$$

The physical meaning of γ_p manifests itself as the resistance to the crack propagation inside the grains and the resistance to propagation through the boundaries. As a result, σ_f is in turn affected by microstructure. The microstructural units controlling the σ_f were different for different steels. The studies in Ref 2, 6, and 7 indicated that the covariant (bainite and/or martensite) packet sizes play decisive roles in controlling the cleavage cracking and the impact toughness in advanced high-strength steels. The high-angle misorientation boundaries in a bainite packet form fine tear ridges on fracture surfaces and provide additional resistance to crack propagation.

The effect of microstructural factors, including prior austenite grain size (PAGS), bainitic/martensitic packet size, distribution of martensite–austenite (MA) constituents, and the density of high-angle grain boundaries (HAGBs), on the DBTT of the steels has been extensively studied. It has been well accepted that the presence of MA constituents increases DBTT (Ref 8, 9). An early study regarding martensitic–bainitic steels (Ref 10) showed that a packet contained many high-angle lath boundaries. However, major cleavage crack deviations occurred only at packet boundaries. Gourgues et al. (Ref 11) and Lambert-Perlade et al. (Ref 12) demonstrated that crystallographic packet, which is separated by high-angle boundaries, is a key microstructural unit in bainitic/martensitic steels for preventing cleavage cracks. Furthermore, Morris et al. (Ref 13, 14) and Tsuboi et al. (Ref 15) proposed that Bain unit boundary could inhibit propagation of cleavage crack in martensitic steels.

The microstructures and mechanical properties in highly ductile low-carbon steel plates with yield strength (YS) greater than 690 MPa have been the subject of extensive investigation

Mi Luo, Dongsheng Liu, and **Binggui Cheng**, Institute of Research of Iron and Steel, Jiangsu Shagang Co. Ltd., Zhangjiagang City 215625, Jiangsu Province, People's Republic of China; and **Rui Cao** and **Jianhong Chen**, State Key Laboratory of Gansu Advanced Processing and Recycling of Non-ferrous Metallic Metals and Key Laboratory of Non-ferrous Metal Alloys of the Ministry of Education, Lanzhou University of Technology, Lanzhou 730050, China. Contact e-mail: dongshengl@hotmail.com.

(Ref 16-26). The as-quenched microstructure which was the base of quenched and tempered microstructure varied being lath martensite (LM), lath bainite (LB), or granular bainite (GB). The microstructural variation depends on chemical composition, thickness of the plate, location across the thickness, and the quenching process. Dhua et al. (Ref 18) achieved desirable LM microstructures in an HSLA-100 steel, which showed balanced Charpy V-notch (CVN) energies and high strength much superior to those of GB microstructure. LB was also a well-accepted as-quenched microstructure in the YS 690 MPa low-carbon alloyed plate (Ref 22). Specimens with the LB exhibited CVN energies higher than 150 J at − 80 °C. This was approximately three times as large as that in specimens with GB. This is attributed to the LB microstructure with higher density of high-angle grain boundaries (HAGBs) and hence smaller effective grain size than those of the GB microstructure. The formation of GB in the steel is in turn due to the limited cooling rates achievable in the core of heavy plates even during quenching. The LB associated with fine MA constituents could be achieved even during slow cooling when appropriate austenitizing process was chosen at as demonstrated by You et al. (Ref 21).

Table 1 Chemical composition of the experimental steel (wt.%)

C	Si	Mn	P	S	Cu	Ni	Cr	Mo	Al	Nb	Ti	N
0.07	0.23	1.06	0.008	0.001	1.25	1.74	0.59	0.485	0.036	0.043	0.019	0.0031

Table 2 Corresponding parameters at different reheating temperatures (T_{RH})

T_{RH}, °C	Max size of asustenite grain, μm	Max size of packet, μm	Density of HAGB, %	Hardness, HV	DBTT, °C	Source
950	42.3	39.5	71	334	− 80	Present work
1000	62.3	31.6	72	334	− 94	Ref 32
1050	67.3	42.0	74	340	− 75	Present work
1100	106.2	53.8	74	344	− 67	Present work
1200	122.3	59.4	72	339	− 56	Ref 32
1250	323.9	95.7	76	338	− 52	Present work

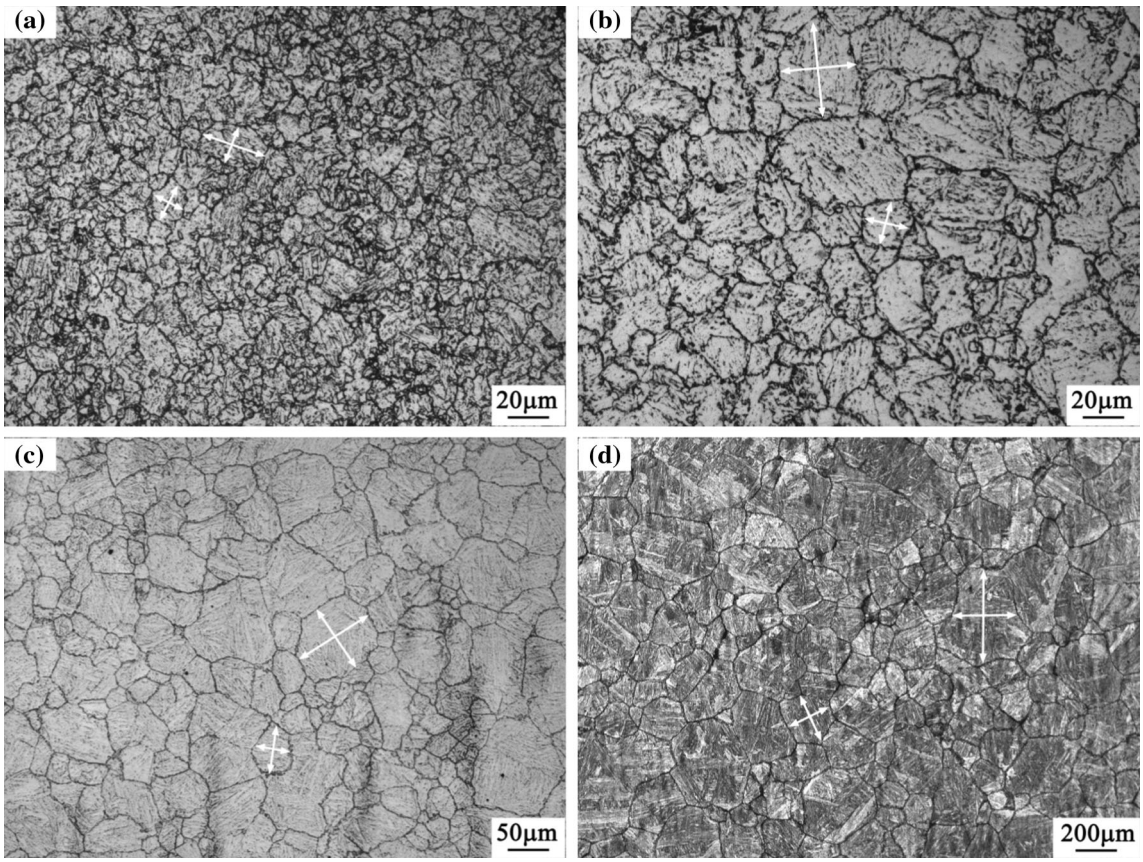

Fig. 1 Optical micrographs showing austenite grains (after picric acid solution etching) and the measurement of the grain size for the specimen austenitized at (a) 950 °C, (b) 1050 °C, (c) 1100 °C, and (d) 1250 °C

Welding is a critical process for the high-strength YS 690 MPa steels (Ref 25-29). The austenite grain size in the coarse-grained heat-affected zone (CGHAZ) may be ten times as large as that in the fine-grained HAZ (FGHAZ) (Ref 25, 30). The Charpy V impact toughness in the parent plate of the F690 steel was approximately 200 J, while that was dramatically deteriorated being only 26 J in the simulated unaltered CGHAZ (Ref 22). All the changes in toughness were associated with the occurrence of cleavage fracture. The local cleavage fracture stress σ_f is regarded as the characteristics of steels and a decisive factor controlling cleavage fracture and toughness (Ref 5, 6, 31). It is therefore essential to study the microstructural factors which can maximize the fracture stress σ_f and hence lower the DBTT in developing advanced highly ductile HSLA steels (Ref 1-3). Systematic investigation on the micromechanism of cleavage fracture behavior in high-strength (YS greater than 690 MPa grade) steels is still inadequate and scarce (Ref 6, 7).

The change in σ_f with microstructural evolution has been studied in an industrially produced low-carbon MnCrMoNiCu plate steel (Ref 32). However, quantitative relationship between σ_f and the microparameters has not yet been established. The present work was to further enrich the database regarding the dependence of DBTT on the microstructures formed in prior austenite with various grain sizes. The fracture behavior on the microstructural variation was studied based on the principles of the micromechanism of cleavage fracture of metal (Ref 5), and finally the dependence of σ_f on the lathy microstructural factors in the investigated steel was established.

2. Experimental Procedures

Blanks of the CVN specimens of dimensions 11 mm × 11 mm × 75 mm were made from an 80-mm-thick plate in the quarter thickness section with their length perpendicular to the rolling direction. The steel was produced by an integrated industrial production process including steelmaking using a basic oxygen furnace, ladle furnace, Ruhrstahl–Heraeus degassing system, and continuous casting, resulting in slabs of thickness 320 mm. The plate was rolled from one of the slabs

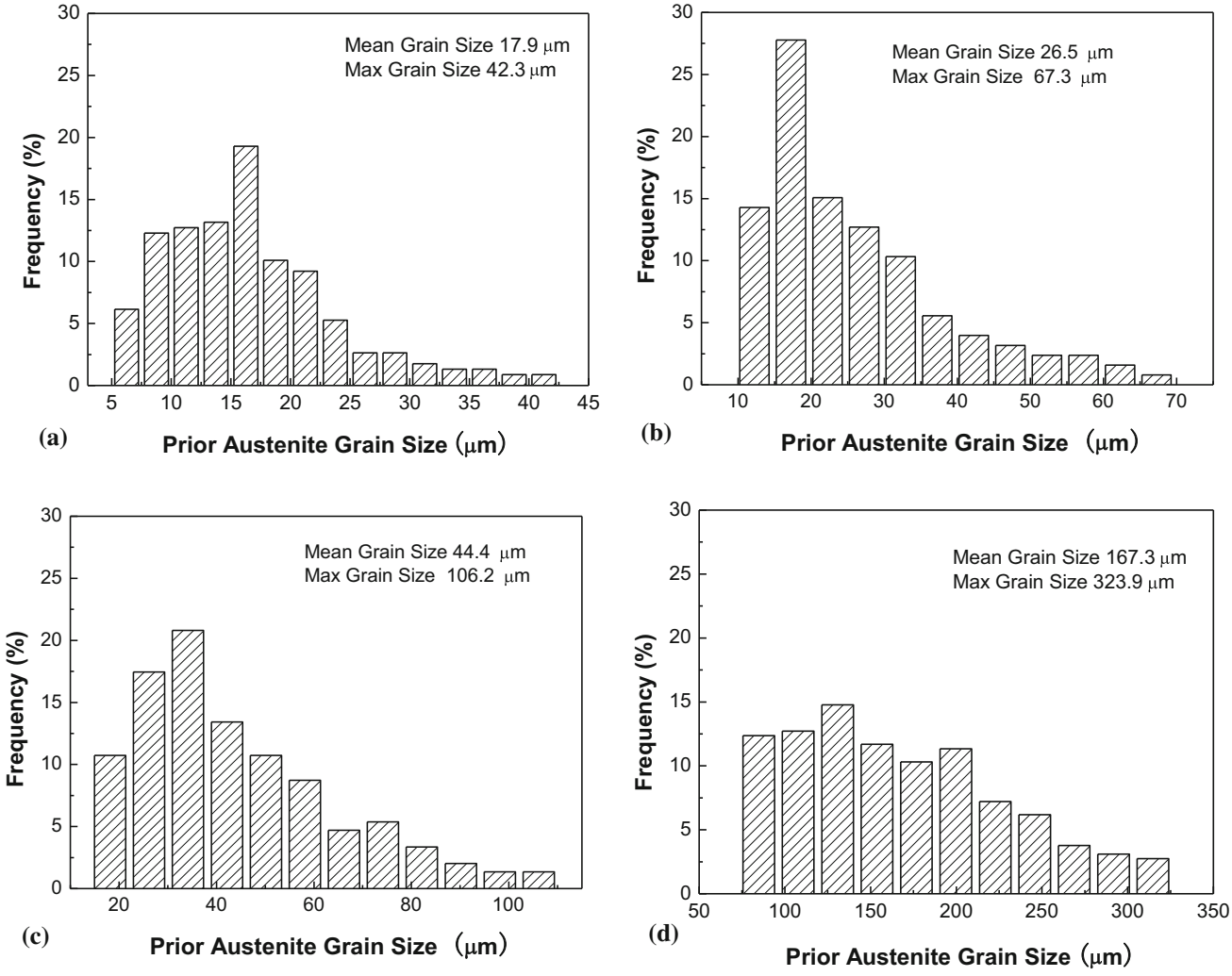

Fig. 2 Austenite grain size distribution of the specimen austenitized at (a) 950 °C, (b) 1050 °C, (c) 1100 °C, and (d) 1250 °C

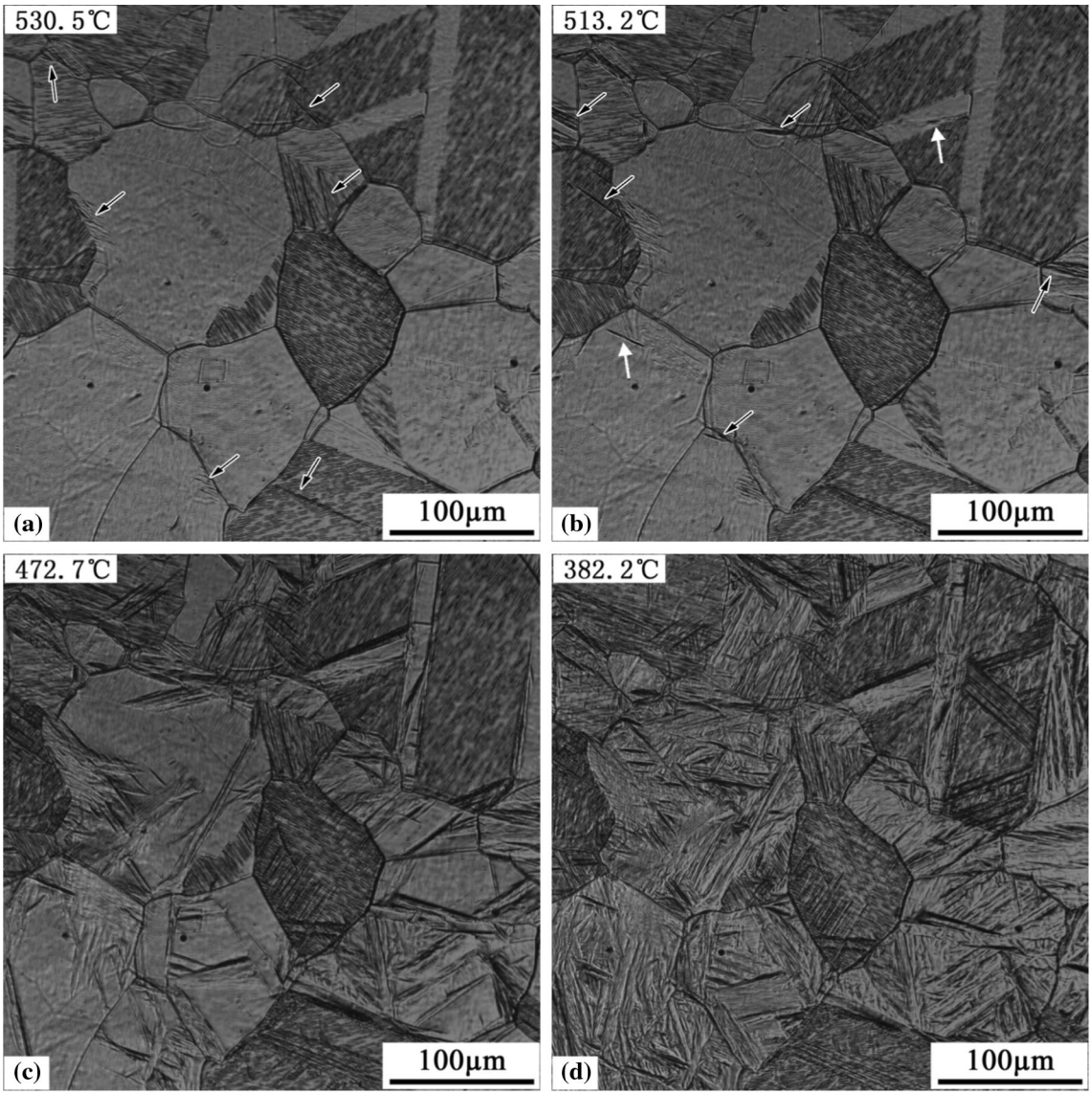

Fig. 3 In situ observation of the morphological evolution showing microstructural change during continuous cooling in the specimen austenitized at 1250 °C

by a 5-m-wide plate mill. After reheating at 1200 °C for 120 min, the slab was subjected to rough rolling, with total reduction ratio of 50%, and finish rolling, again with a total reduction ratio of 50% at austenite recrystallization and non-recrystallization regions, respectively (Ref 22). The chemical composition of the steel is given in Table 1.

Thermal simulations were performed using a Gleeble 3800 thermomechanical simulator (Dynamic System Inc, Poestenkill, NY). A Pt-10 pct Rh thermocouple was spot-welded in the middle along the length of the specimens for recording the temperature. Each specimen was heated at 5 °C/s up to predetermined temperatures of 950, 1050, 1100, or 1250 °C, held there for 5 min, and then continuously cooled at 5 °C/s down to 500 °C followed by a continuous cooling transformation (CCT) at 2.5 °C/s to room temperature.

The as-quenched samples were cross-sectioned, and the plane coinciding with the thermocouple position was ground and polished by the conventional technique. Saturated aqueous picric acid was used to reveal the austenite grain boundaries at 338 ± 5 K (65 ± 5 °C). A Nital reagent composed of 4% nitric acid in denatured ethanol was used to reveal the transformed microstructures. The austenite grain size or bainitic/martensitic packet size was measured as the average value of the two diameters perpendicular to each other using an optical microscope. The individual packets were characterized based on the morphology or growth orientation of ferrite laths. The transformed microstructures at room temperature were further observed with a scanning electron microscope (SEM), FEI's model Quanta 3D FEG. Electron backscatter diffraction (EBSD) analysis (resolution 0.1 μm) was performed by employing a field emission SEM (model: JSM-7001F) equipped with an EBSD camera. The data were then interpreted by HKL technology Channel 5 software. These samples were also subjected to Vickers hardness testing using a 10-kg load. A more detailed metallographic examination was performed on selected specimens using a TEM (model: JEM-2100F) equipped with energy-dispersive spectrometry (EDS) attachment. Thin foils for TEM observations (at 200 kV) were

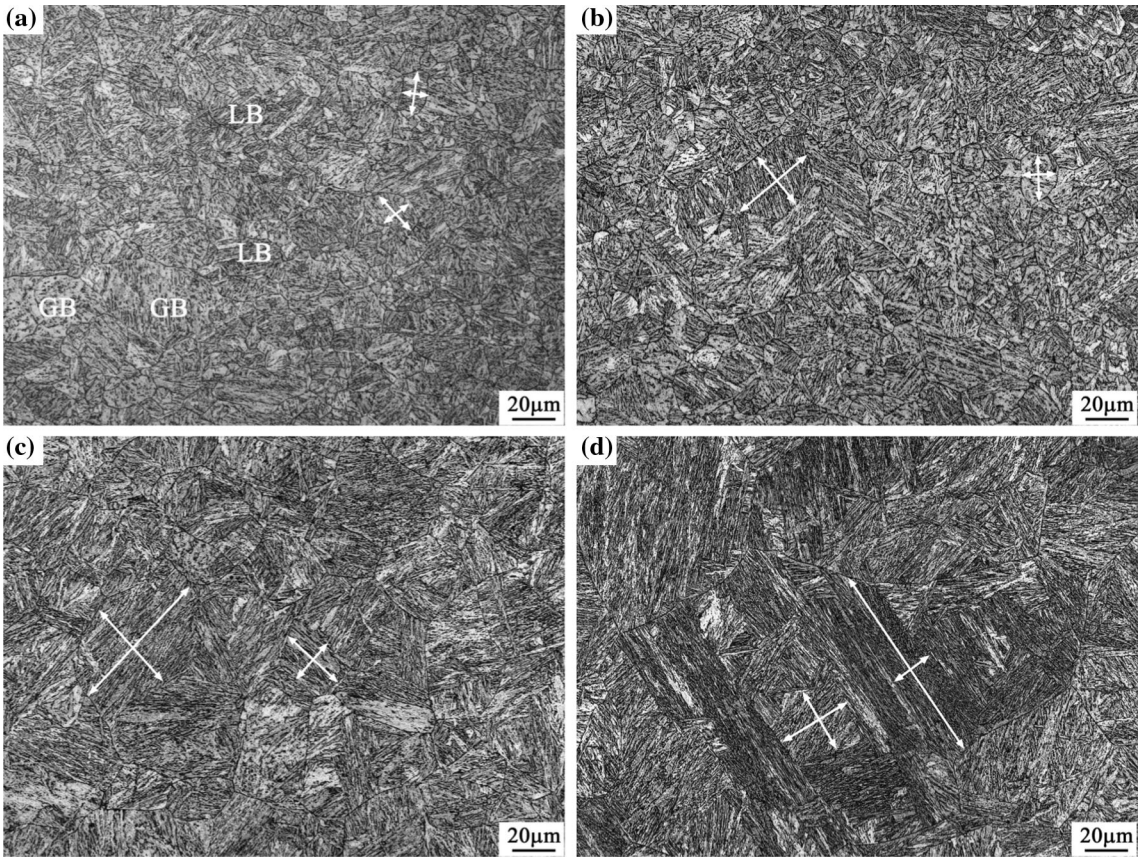

Fig. 4 Morphologies as observed under an optical microscope (after 4% Nital etching) and measurement of packet size for the specimens austenitized at (a) 950 °C, (b) 1050 °C, (c) 1100 °C, and (d) 1250 °C

prepared in a twin-jet electrolytic apparatus using a solution containing 5 vol.% perchloric acid and 95 vol.% ethanol.

To do an in situ observation on microstructure evolution during CCT, a sample was sectioned from the plate and machined into a disk (3.8 mm diameter × 3 mm height), mirror-polished and set into a high-purity alumina crucible (4.5 mm inner dia. × 5 mm height). The microstructure during heating was observed by a confocal scanning laser microscope (CSLM) (Ref 33). The sample and crucible were placed into the gold image furnace and heated at 5 °C/s to desired temperatures in high-purity argon, preventing any oxidation. The microstructural change with the aforementioned temperature and time was observed and recorded for final analysis.

Standard CVN specimens (10 mm × 10 mm × 55 mm) were prepared with the V-notch parallel to the direction of thickness at the position of the spot-welded thermocouple. Impact energy was measured at room temperature, − 20, − 60, − 85, − 100, − 120, − 196 °C by employing a 450-J instrumented pendulum impact tester (model IMP450 J Dynatup, Instron) with a tup striker of radius 2 mm. The load and the absorbed energy pertaining to the displacement curves measured by the instrumented Charpy V impact tester were recorded for further analysis. The global dynamic yield strength σ_{dy} can be calculated from the measured dynamic yield load P_y by the following formula (Ref 34):

$$\sigma_{dy} = 2.99P_yW/B(W-a)^2, \quad \text{(Eq 3)}$$

where W is the width, B the thickness, and a the notch depth of specimen.The fracture surfaces of failed Charpy V specimens were observed in detail by the SEM. The relative microscopic parameters were measured for analyzing the micromechanism of fracture. The fracture surface may consist of (1) an original notch, (2) a stretch zone (SZW), which is actually produced by blunting the original notch root and is characterized by a smooth formless pattern, (3) an area of ductile fracture with a fine dimple pattern, in which a fibrous crack length (SCL) could be measured, and (4) a cleavage cracking zone (CCZ) that shows several cleavage facets with river pattern strips on them. The fracture distance X_f is the distance from the site of cleavage crack initiation to the blunted notch tip or fibrous crack. The cleavage initiation site was located by tracing back the river pattern strips to their origins, and X_f was measured. The SZW, SCL, and CCZ present an integrated cracking process. The details of the methodology to measure the SZW, SCL, or X_f have been documented in the literature (Ref 5, 31). To find the cracks retained in failed specimens, the cross sections perpendicular to both the fracture surface and length direction of the V-notch were polished, etched by the Nital solution, and examined under the optical microscope and SEM.

3. Experimental Results

3.1 Prior Austenite Microstructure at Austenitizing Temperature

For a 5-min hold at different temperatures, the sizes of the mean or coarsest prior austenite grains increased as the austenitizing temperature was raised, being 17.9 or 42.3 μm at 950 °C, 26.5 or 67.3 μm at 1050 °C, and 44.4 or 106.2 μm at 1100 °C. A dramatic increase in the mean grain size 167.3 μm associated with the coarsest grain size of 323.9 μm was observed when the reheat temperature was raised to 1250 °C (listed in Table 2). Figure 1 shows the original austenite grains observed in the specimens with austenitizing temperatures of 950, 1050, 1100, and 1250 °C. Figure 2 summarizes reheat conditions and associated distributions of austenite grain sizes.

3.2 In Situ Observation on Austenite-to-Bainite/Martensite Transformation

Microstructural evolution in the specimen austenitized at 1250 °C is displayed in Fig. 3. Lath-like grain boundary ferrite which mainly nucleated on the prior austenite grain boundaries was observed as indicated by black arrows. In addition, minor intragranular nucleation (indicated by white arrows) transformation mechanism was also observed. The grain boundary ferrites grow in the same direction parallel to each other. Although the growth of the grain boundary ferrite can also cause impingement each other, the microstructure seems orderly. Previous study (Ref 32) found that grain boundary nucleation was the common mechanism at the start of the transformation. The impingement of ferritic laths is absent when the PAGS is small; however, it occurs when the austenite grain size becomes larger. This study also showed that the coarse austenite grain was fragmented, resulting in a few packets due to the impingement (Fig. 3d).

3.3 Resultant Microstructures After Continuous Cooling Transformation

The change in microstructure with austenitizing temperature during the transformation was qualitatively or quantitatively characterized. Optical morphologies of resultant microstructures at room temperature in specimens austenitized at 950, 1050, 1100, and 1250 °C are shown in Fig. 4, respectively. Figure 5 shows the decrease in size or fraction of the MA constituents as the austenitizing temperature is raised. SEM images of the corresponding specimens are shown in Fig. 6. The microstructure in the specimen austenitized at 950 °C is a mixture of LB + GB + LM, and that austenitized at 1050 °C is mainly a mixture of LB + LM with refined MA constituents on the lath boundaries. The microstructure in the specimen austenitized at 1100 or 1250 °C is also dominated by LB + LM. The maximum packet size, however, increased with increase in austenitizing temperature being 39.5, 42.0, 53.8, and

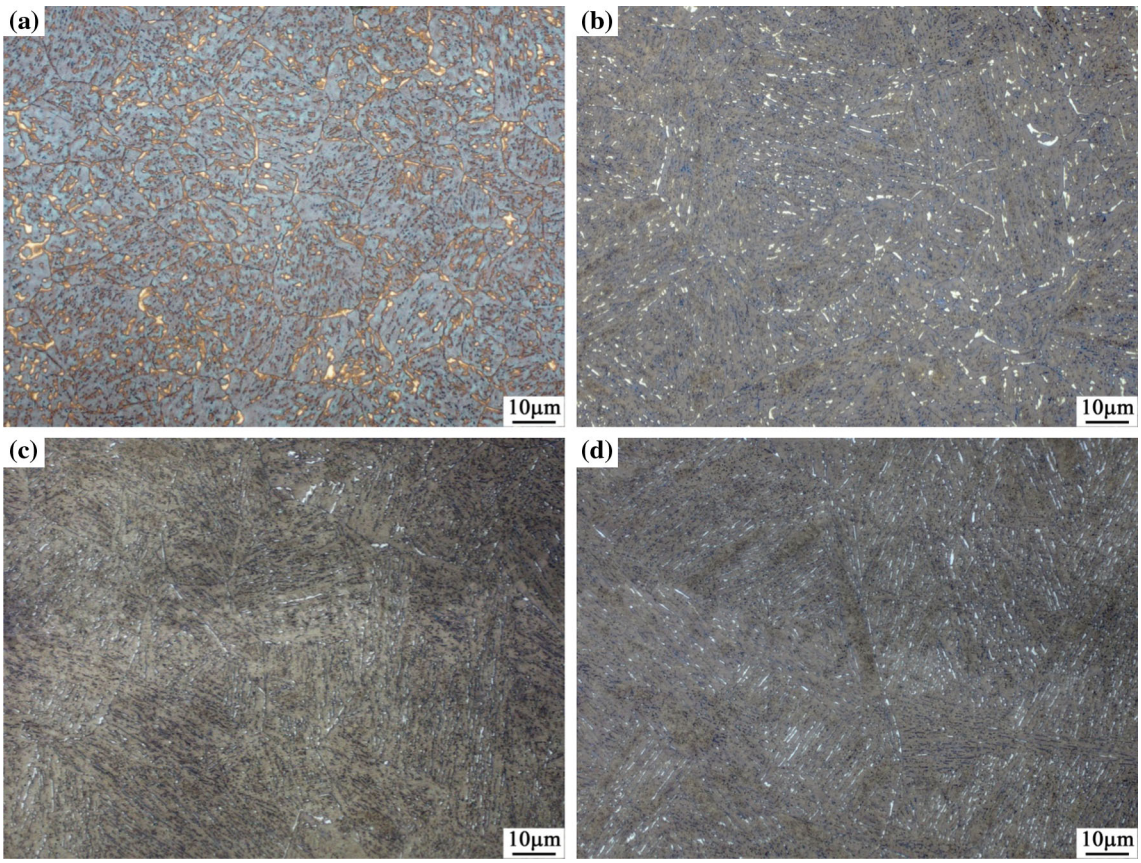

Fig. 5 Morphologies as observed under an optical microscope (LePera reagent) for the specimens austenitized at (a) 950 °C, (b) 1050 °C, (c) 1100 °C, and (d) 1250 °C, showing a white phase corresponding to the MA constituents

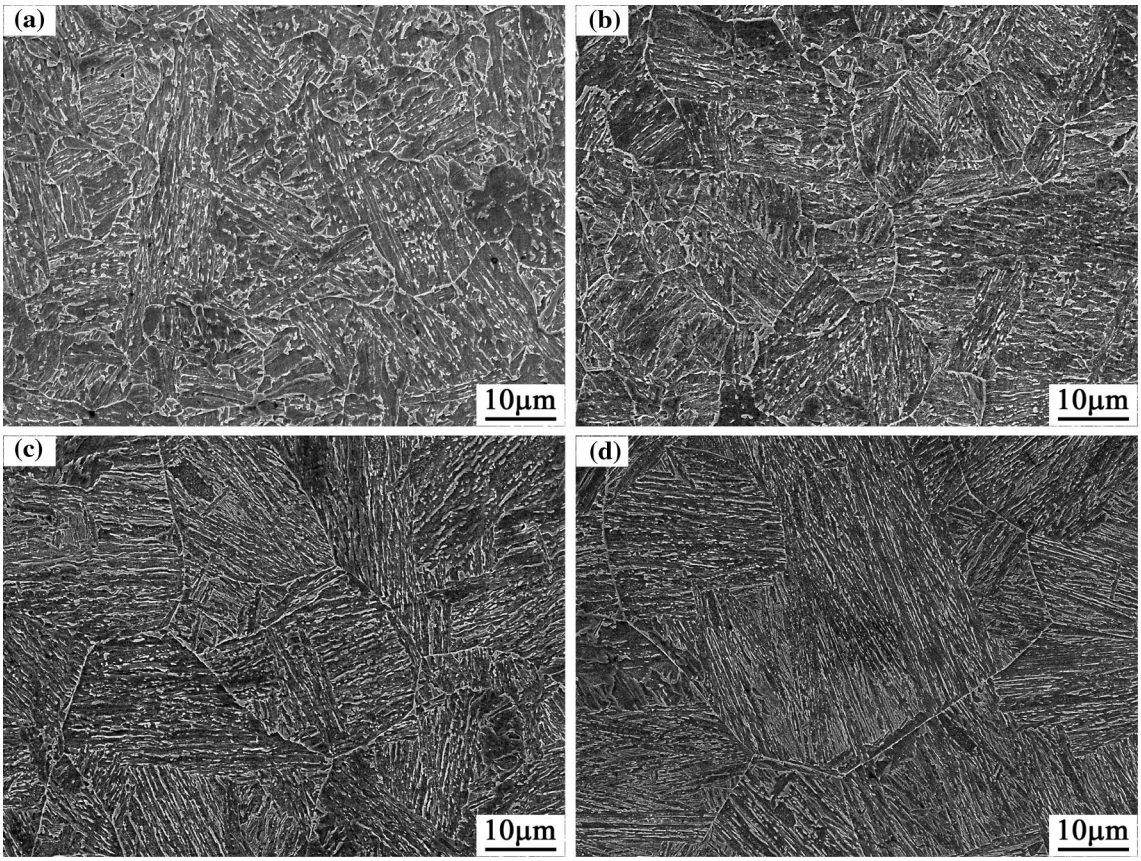

Fig. 6 SEM images of the specimens (4% Nital etching) austenitized at (a) 950 °C, (b) 1050 °C, (c) 1100 °C, and (d) 1250 °C

95.7 μm for 950, 1050, 1100, and 1250 °C, respectively (listed in Table 2). The corresponding frequency distributions of packet sizes in all the conditions are shown in Fig. 7. In the case austenitizing at 950 °C, one austenite grain approximately transforms into one bainite packet. With increase in austenite grain size, one coarsened austenite grain transforms into a numbers of LM/LB packets (Ref 35).

Figure 8 shows the TEM images of the specimens austenitized at different temperatures. Autotempered martensite laths and lower bainite were indentified in the specimen austenitized at 950 °C (Fig. 8a and b). Autotempered laths of martensite with tangled dislocations were observed in the specimens austenitized at 1100 and 1250 °C (Fig. 8c-f).

Figure 9 exhibits EBSD maps showing HAGB (greater than 15°) in the specimens austenitized at different temperatures with different prior austenite grain sizes. It can be seen that the boundaries of prior austenite grains, the boundaries of the covariant packets, and some interlath boundaries within the packets parallel to each other are featured by HAGBs.

3.4 Charpy V Impact Testing and the Curves of Load–Energy Versus Displacement

Figure 10 shows the variation of the absorbed energy versus austenitizing temperature. Testing at − 20 and −60 °C, similar impact toughness levels were achieved in the specimens austenitized at 950 and 1050 °C. The impact toughness decreased continuously as the austenitizing temperature increased further. Figure 11 presents the ductile-to-brittle transition curves. The DBTT, which is defined as the temperature corresponding to the average value of the upper-shelf and lower-shelf energies, was characterized as − 80, − 67, and − 52 °C for the austenitizing temperatures at 950, 1100, and 1250 °C, respectively. The DBTT of the specimen austenitized at 1050 °C was determined as − 75 °C. Here, the toughness is maximized in the specimen austenitized at 950 °C with the LB + GB + LM microstructures.

The characteristics of the fractures in the fully ductile upper-shelf region, ductile-to-brittle transition region, and lower-shelf region, are reflected in the curves of the CVN impact load combined with the impact energy versus hammer displacement, as shown in Fig. 12. In the upper-shelf region, the absorbed energy decreased as austenitizing temperature increased, which may be attributed to the decrease in plasticity as prior austenite grain size increased (Fig. 12a and b) (Ref 31). The fracture at −60 °C was still fully ductile in the specimen austenitized at 950 °C (Fig. 12c), and it was a mixture of ductile and brittle failures at − 85 °C (Fig. 12d). The decrease in crack propagation energy and the total impact energy with the reduction in the extension length for fibrous crack propagation is obvious for specimens fractured in the transition region (Fig. 12d-g). All the specimens tested at − 196 °C were fractured in brittle cleavage mode, whereas the fracture load P_f decreased as the austenitizing temperature increased (see Fig. 12h and Table 3).

3.5 Fractographs of the Failed Charpy V Specimens

Representative SEM fractographs of the CVN samples fractured at ductile-to-brittle transition region are presented in Fig. 13. Fibrous crack propagation proceeded before the

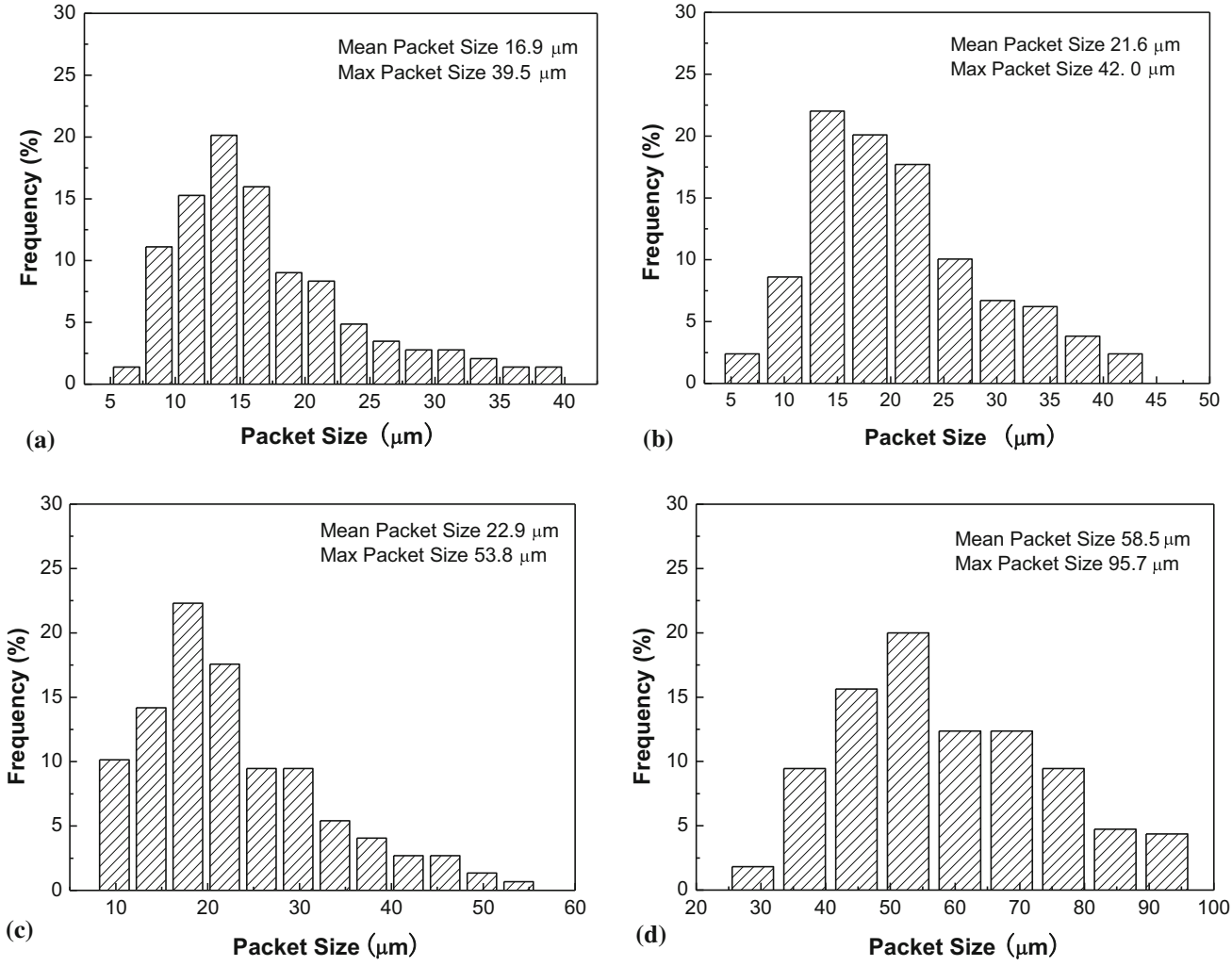

Fig. 7 Histograms of packet sizes of the specimens austenitized at (a) 950 °C, (b) 1050 °C, (c) 1100 °C, and (d) 1250 °C

cleavage crack was triggered. As a result, the fracture surface is consisted of ductile fracture (fibrous crack propagation) and brittle fracture regions. The total absorbed energy E_t increases as the fibrous crack propagation width (SZW + SCL) increases, regardless the processing conditions (indicated in Table 4). This is consistent with previous reports (Ref 31, 36). Note that the ductile-to-brittle transition is postponed to the lowest temperatures to − 120 °C in the specimen austenitized at 950 °C (Fig. 13f).

The fractographs of the specimens that failed in the brittle mode in the lower-shelf region are displayed in Fig. 14. A microcrack may be initiated from a second-phase particle, which then propagates across a bainite/martensite high-angle packet boundary, leading to final failure. The origins and path ways of the microcrack propagation are indicated by the arrows. The size of the cleavage fracture facet at the origin of the cleavage crack (a_f) changes in the order consistent with the order of the packets' sizes. The value of a_f was measured by averaging the lengths of two diameters perpendicular to each other covering the area of interest. The coarse tear ridges are the packets' boundaries, which act as the main barriers against the brittle crack propagation (Ref 6). Here, the density of coarse tear ridges seems decrease dramatically as the bainite/martensite packet size increases. The parallel fine tear ridges within the cleavage facet can be attributed to the interlath boundaries with high misorientations (Ref 6). By identifying the crack initiation site, cleavage fracture distance X_f is measured (listed in Table 3).

3.6 Critical Event for the Cleavage Fracture

The cleavage microcracking is composed of (1) crack nucleation, (2) crack propagation across the particle–grain boundary, and (3) crack propagation across the grain–grain boundary (Ref 11). It is essential to identify which one of the above three stages is the greatest difficulty, i.e., the critical event, in the formation of a cleavage crack. Figure 15 exhibits the crack retained in the specimens with different microstructures. The retained cracks are constrained in a packet, and their further propagation is inhibited at the packet boundaries. As a result, the propagation of a grain-sized crack into contiguous grains is the critical event for cleavage fracture in the notched specimens of the high-strength 690 MPa grade steel.

3.7 Estimated Fracture Stress σ_f

The yield stress σ_{dy} and yield load P_y for specimen fractured at − 196 °C were calculated by extrapolating the experimental data at the high test temperatures (Ref 32). Using the measured

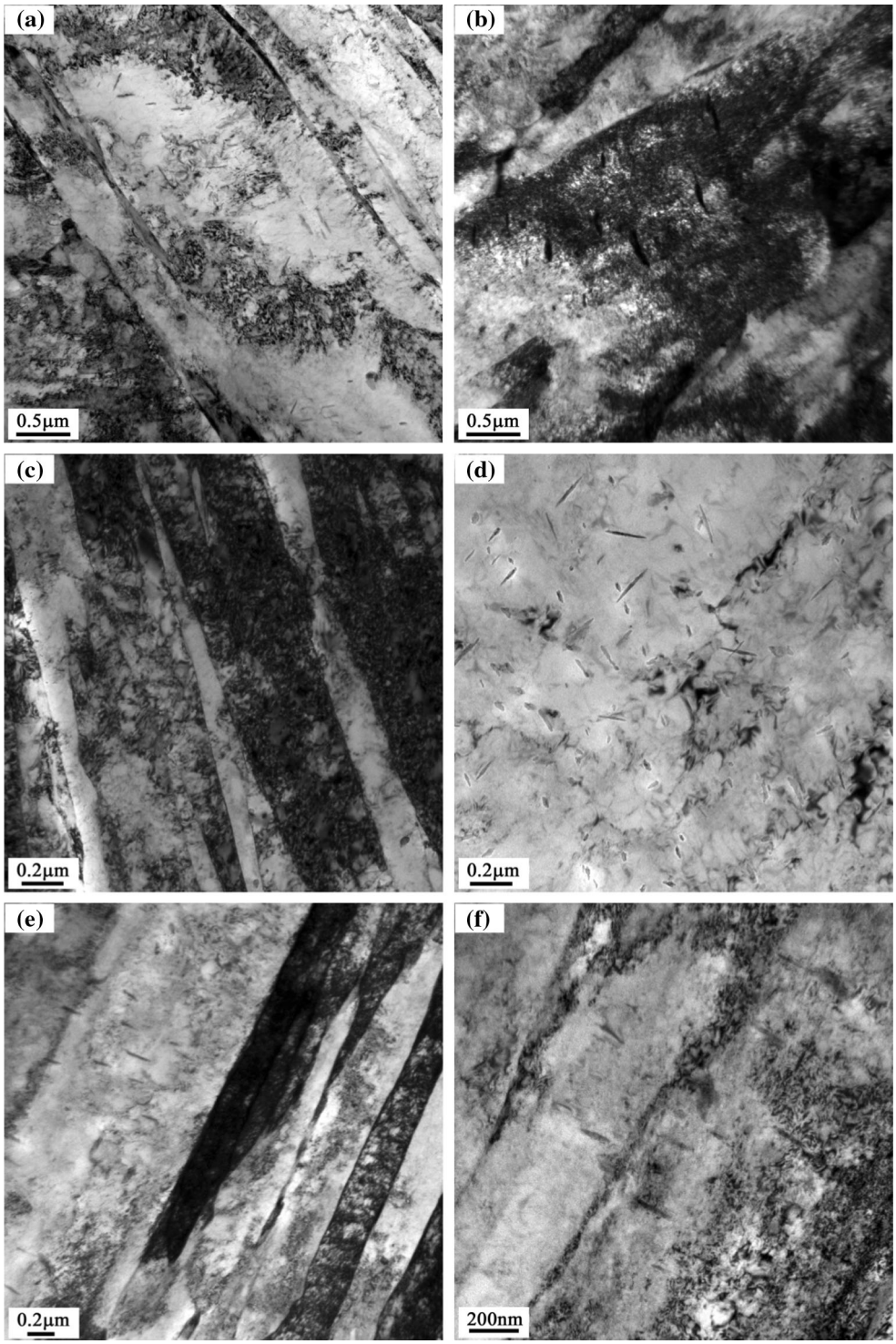

Fig. 8 Thin foil TEM images of specimens austenitized at (a) and (b) 950 °C, (c) and (d) 1100 °C, (e) and (f) 1250 °C

fracture load (P_f) and the dynamic yield load P_y at −196 °C, suitable distribution curves of stress, strain, and stress triaxiality ahead of the notch were calculated using the finite element method (FEM) (Ref 6, 31, 32). The results of the FEM are displayed in Fig. 16. From the measured X_f, the corresponding values of ordinates on the curves of stress, strain, and stress triaxiality are taken as the local cleavage fracture stress σ_f, the fracture strain ε_{pc}, and the critical stress triaxiality T_c, respectively. The values of the microparameters are listed in Table 3. The average unit crack path (UCP) or packet size (d_p) was used in calculating γ_p in the literature, as shown by Eq 2 (Ref 2, 7). The ratio of UCP to d_p is approximately 1.2-1.5 for bainitic and martensitic steels (Ref 7). However, the present authors believe that a_f may better represent the real size of the initial crack

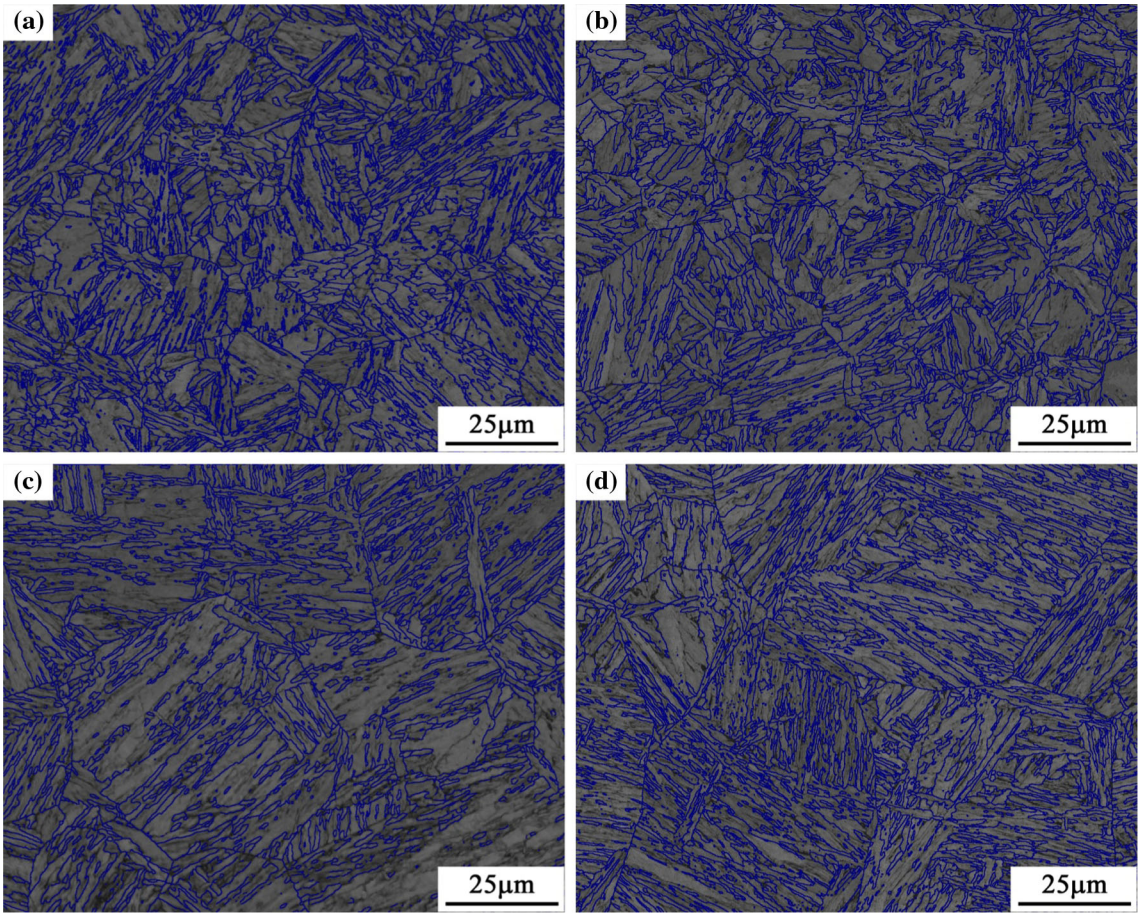

Fig. 9 EBSD maps of the specimens austenitized at (a) 950 °C, (b) 1050 °C, (c) 1100 °C, and (d) 1250 °C (thick lines are the grain boundaries with misorientation greater than 15°)

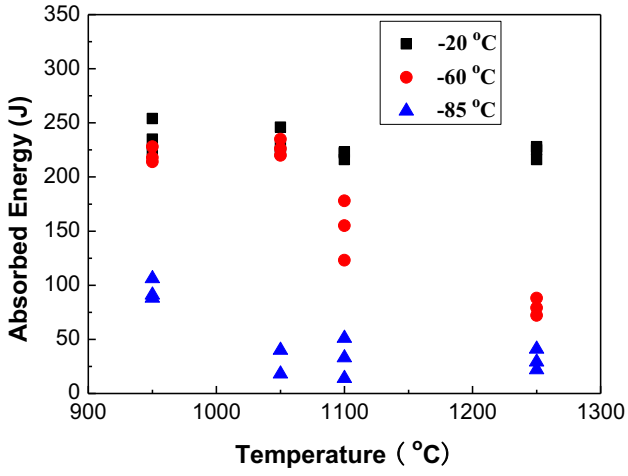

Fig. 10 Variation of the Charpy V impact energy vs. austenitizing temperature

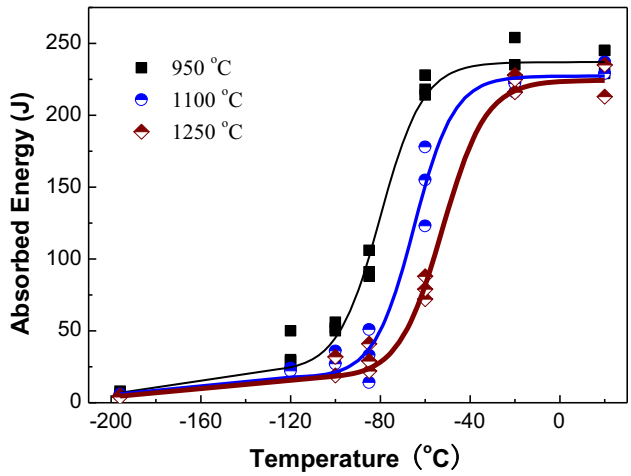

Fig. 11 Ductile-to-brittle transition curves for specimens austenitized at 950, 1100, and 1250 °C as indicated

nucleus (Ref 6, 31, 32). Based on the measured σ_f, and used a_f to replace d_p in formula (2), the effective surface energy γ_p were calculated for the specimens austenitized at 950, 1100, and 1250 °C, respectively. The values of calculated γ_p are also listed in Table 3.

The microstructural factors and microparameters for cleavage fracture in specimens austenitized at 1000 and 1200 °C were achieved in our previous work (Ref 32) for the test steel (listed in Tables 2 and 3). As a result, a linear relationship between σ_f and a_f should be established here. Figure 17 shows

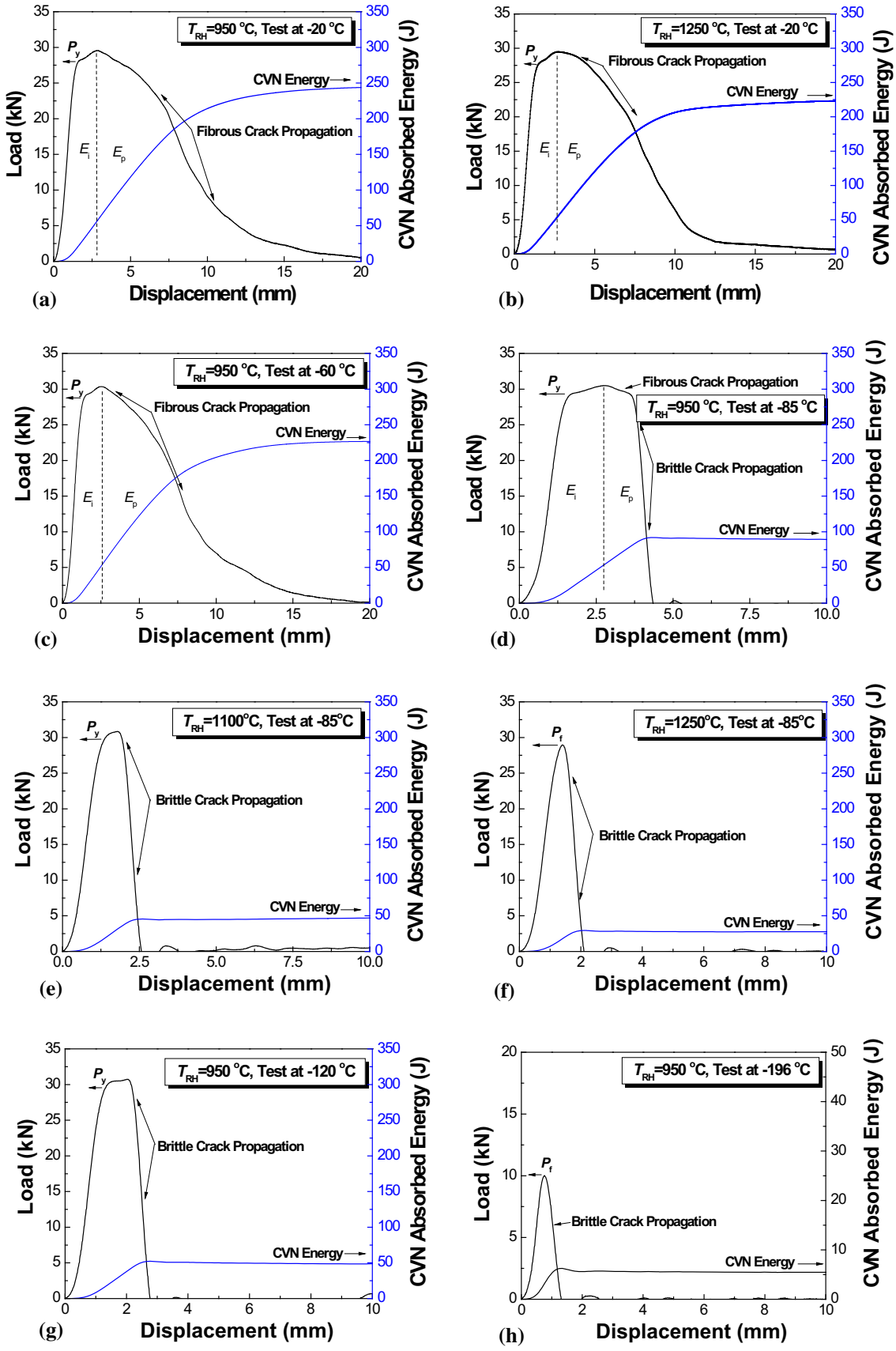

Fig. 12 Curves of load and Charpy impact energy vs. hammer displacement obtained in the instrumented impact tests conducted for specimens with different austenitizing temperatures (T_{RH}) and tested at different temperatures as indicated

Table 3 Microparameters for cleavage fracture at − 196 °C

T_{RH}, °C	a_f, μm	P_f, kN	P_y, kN	P_f/P_y	σ_{dy}, MPa	X_f, μm	σ_f, MPa	ε_{pc}	T_c	Q_c (σ_f/σ_{dy})	γ_p, J/m^2	Source
950	39.4	10.01	32.13	0.311	1501	120.0	2401	0.010	0.94	1.60	328	Present
1000	33.0	16.70	32.49	0.514	1518	295.0	2868	0.004	1.21	1.89	393	Ref 32
1050	40.0		32.60		1523	197.2	2314			1.52	310	Present
1100	45.0	8.40	32.80	0.256	1532	41.0	1975	0.005	0.22	1.29	254	Present
1200	45.1	7.90	32.00	0.247	1454	50.0	1908	0.004	0.22	1.27	237	Ref 32
1250	46.4	6.80	31.83	0.214	1487	41.0	1833	0.001	0.19	1.26	226	Present

a_f, cleavage facet size around the crack initiation site; σ_{dy}, dynamic yield strength; σ_f, local cleavage fracture stress; ε_{pc}, fracture strain; T_C, critical stress triaxiality; Q_C, critical stress intensification factor; γ_p, effective surface energy; P_f , fracture load; X_f, critical distance of cleavage

the dependence of σ_f upon a_f. The microparameters including σ_f of the specimen austenitized at 1050 °C were then determined (listed in Table 3).

4. Discussion

4.1 Effect of Austenitizing Condition on Microstructural Evolution

The austenite grain size increases as the austenitizing temperature is raised. The austenite grain boundaries could be pinned by Nb carbides and TiN particles during the austenitizing processes at 950-1100 °C; the grain boundaries, however, should be mainly pinned by TiN particles at 1250 °C. According to Table 1, the atomic fraction (at.%) of nitrogen in the investigated steel is 0.012 at.%, and the atomic fraction for Ti is 0.023 at.%. As nitrogen is much more stable in TiN than in NbCN, the whole content of N would be devoted to TiN in this test steel. The evolution of microalloyed precipitates associated with the austenitizing process is therefore mainly related with NbC. The sluggish grain growth in the low range of austenitizing temperatures (950-1100 °C) can be attributed to the existence of NbC precipitates that affected the grain growth by providing pinning forces to the grain boundaries. The precipitates would be gradually dissolved in the austenite or coarsened as the austenitizing temperature is raised (Ref 30), thereby the pinning effect would be reduced, and the grain growth is thus promoted. The substantial grain growth at 1250 °C can be attributed to the complete dissolution of Nb-rich carbide precipitates in the austenite (Ref 22, 23). In this case, only TiN precipitates can survive at 1250 °C affecting the austenite grain growth, also by providing pinning forces.

The transformed microstructure at room temperature varied with austenitizing temperature being LB + GB + LM mixture corresponding to the austenitizing temperature of 950 °C, and LB + LM to 1050, 1100, and 1250 °C, respectively. The packet sizes of the two variants increased as the austenitizing temperature increased. Grain boundary nucleation was found during cooling at the start of phase transformation as the main mechanism in above cases. The reason of the microstructural change is attributed to the increase in hardenability associated with the increase in the austenite grain size as the austenitizing temperature is raised.

Previous works showed that the temperature of austenitizing that causes substantial dissolution of niobium carbonitride precipitates varies with the content of Nb and thermal history. Shome et al. (Ref 37) calculated and confirmed that rapid dissolution of the precipitates takes place above 1168 °C for a simulated welding thermal cycle with heat input of 10 kJ/cm and 1146 °C for 40 kJ/cm, respectively, for a HSLA-100 steel with 0.029 wt.% Nb. Isothermal austenitizing at 950 °C would result in complete dissolution of Cu-containing precipitate (if any presences prior to the reheating); however, it is speculated that NbC precipitates would remain undissolved based on the work by Spanos et al. (Ref 25). The increased hardenability of the austenite is attributed to (1) reduced portion of austenite grain boundaries because of the grain coarsening as shown in Fig. 1 and 2, and (2) a substantial dissolution of NbC precipitates at the high temperatures.

4.2 Microstructural Factors Affecting the Brittle Fracture Stress σ_f and Brittle Fracture Behavior

The fracture stress σ_f and DBTT of the specimen austenitized at 950 °C are a result of the mixture microstructure (LB + GB + LM). The fine LB and LM are desired microstructures that always make σ_f higher and the DBTT lower. The effect of GB on σ_f and the DBTT is different from that of LB + LM. The decrease in σ_f or the increase in DBTT with the increase in the austenitizing temperature is, however, mainly attributed to the increased packet size. This is attributed to the fact that the MA fraction is reduced as the austenitizing temperature is raised.

The HAGBs detected included prior austenite grain boundaries, packet boundaries, and the interlath high-angle boundaries in the packets that are parallel to each other. A packet should be enclosed by the first two types of boundaries. According to the present observations, the packet boundaries play controlling roles, on which the way of crack propagation is inhibited and thus the resistance of crack propagation is increased (Fig. 15). In fact, σ_f is offered by the weakest microstructural component (Ref 5). a_f value thus increases as the sizes of the coarsest packets increase. As a result, the local fracture stress σ_f changes in the order from high to low being 2401, 2314, 1975, and 1833 MPa (Table 3) also in the increased order of the largest packets' size corresponding to specimens austenitized at 950, 1050, 1100, and 1250 °C, respectively. This analysis is consistent with the recent work (Ref 9), which showed that the size of the coarsest grains in the effective grain size distribution at 80th percentile was the critical unit size for the cleavage fracture in the martensitic and bainitic steels. Furthermore, the high-angle misorientation boundaries in a bainite/martensite packet form parallel fine tear ridges on fracture surfaces and provide additional resistance, rather than the decisive barriers, to the crack propagation (Fig. 14).

According to the Yoffee diagram, the brittle fracture occurs when the yield stress (σ_Y) exceeds the cleavage fracture stress σ_f (Ref 1-3). The DBTT changes from low to high tempera-

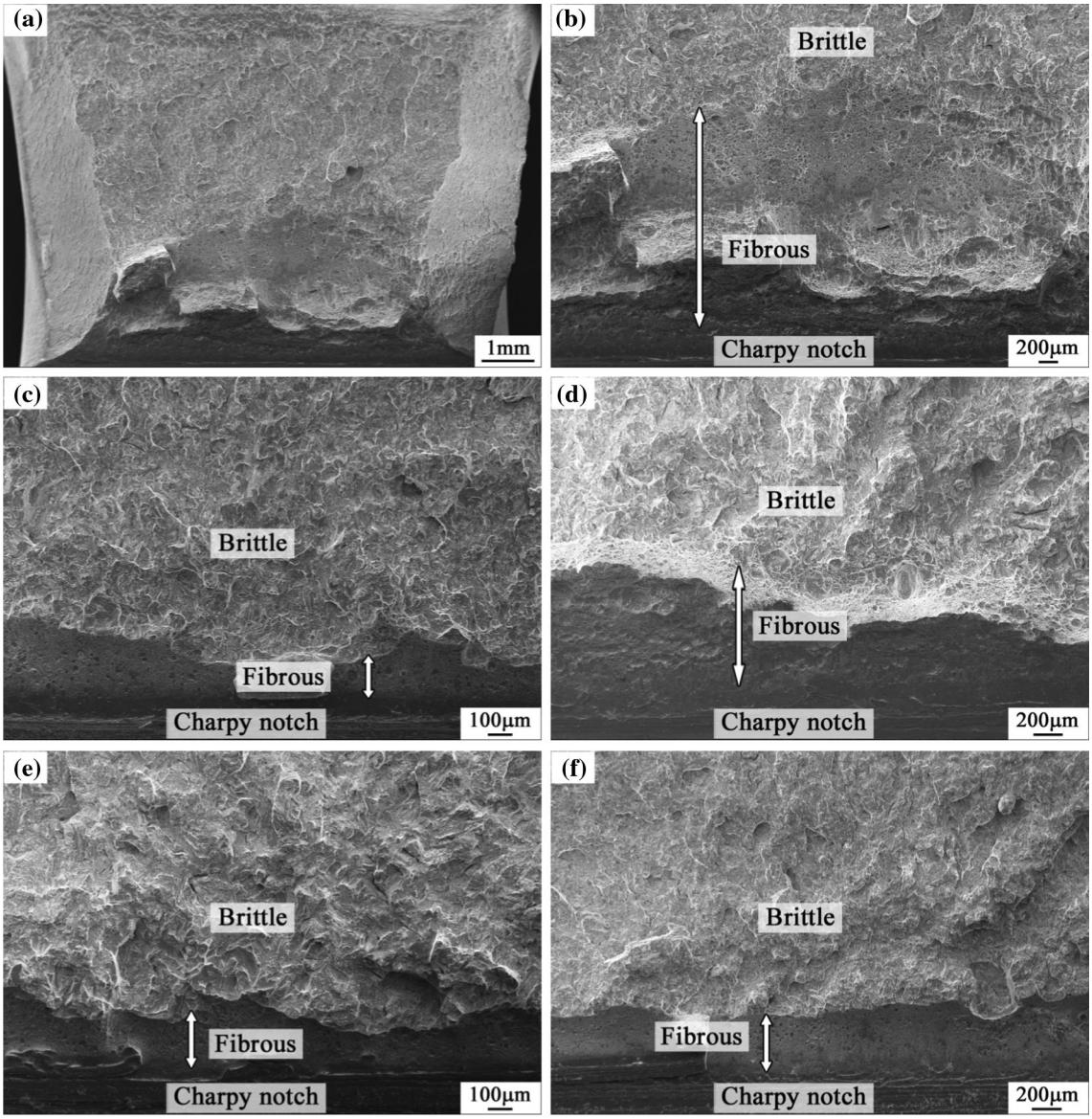

Fig. 13 SEM morphologies showing fracture surfaces of the failed Charpy specimens in ductile-to-brittle transition region as: (a) and (b) austenitized at 1100 °C and failed at − 60 °C, (c) austenitized at 1100 °C and failed at − 85 °C, (d) austenitized at 1250 °C and failed at − 60 °C, (e) austenitized at 1250 °C and failed at − 85 °C, (f) austenitized at 950 °C and failed at − 120 °C

Table 4 Microparameters for fracture at ductile-to-brittle transition region

T_{RH}, °C	Test Temp., °C	E_t, J	SZW, μm	SCL, μm	SZW + SCL, μm
1100	− 60	153	193.5	2456.3	2649.8
1100	− 85	27	109.4	294.8	404.2
1250	− 60	79	183.1	819.2	1002.3
1250	− 85	21	94.2	218.4	312.6
950	− 120	28	111.1	334.4	445.5

tures, being − 80, − 67, and − 52 °C (Table 2) corresponding the order of σ_f. In the cases of impact loading on the *V*-notched specimens, the criterion for triggering cleavage crack is expressed as:

$$\sigma_{yy} \geq \sigma_f, \quad \text{(Eq 4)}$$

where the σ_{yy} is the normal stress ahead of the notch root which is intensified from the σ_{dy} through the formula $\sigma_{yy} = Q\sigma_{dy}$. At cleavage cracking, the stress intensification factor $Q = \sigma_{yy}/\sigma_{dy}$ evolves to the critical value $Q_c = \sigma_f/\sigma_{dy}$. The higher Q_c means more plastic strain is needed to be produced to intensify the normal stress σ_{yy} to σ_f. The decrease in σ_f makes the cleavage fracture easier and increase the DBTT. It also makes the termination of the extension of the fibrous crack early and cuts down its length, thus decreases the toughness in the transition temperature region (Ref 5, 31).

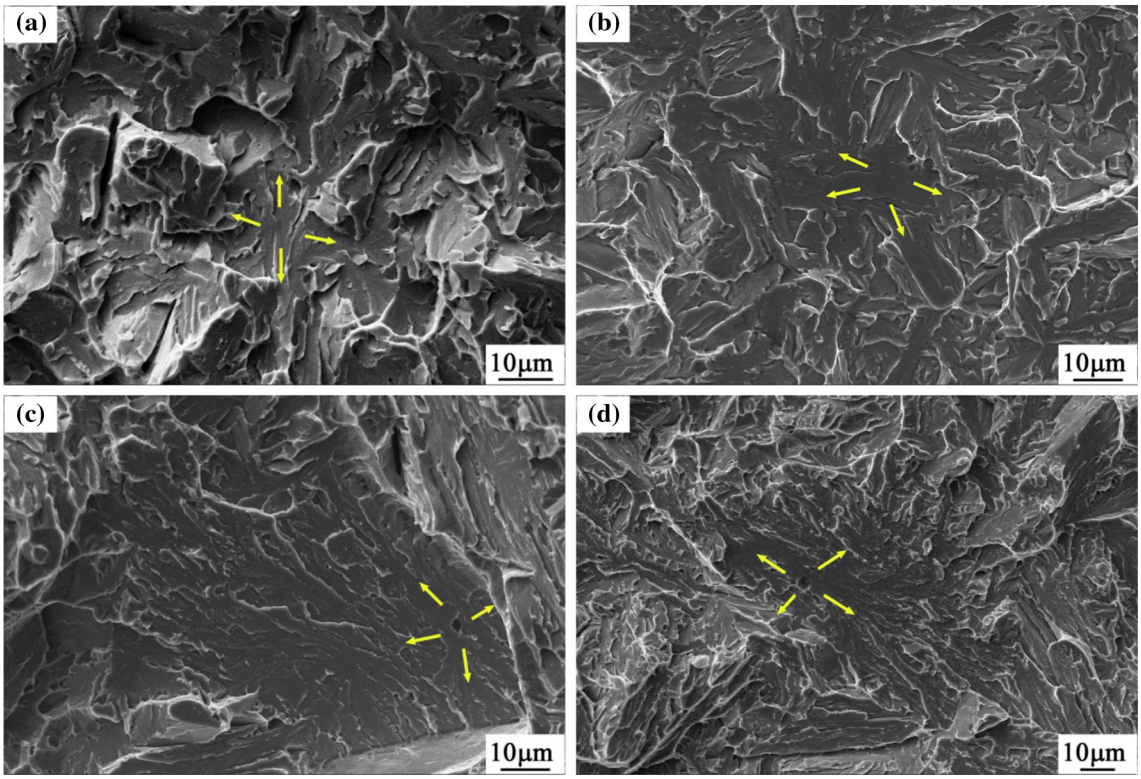

Fig. 14 SEM morphology showing fracture surface near the crack initiation site of a Charpy V specimen austenitized at (a) 950 °C, (b) 1050 °C, (c) 1100 °C, and (d) 1250 °C, all failed at − 196 °C

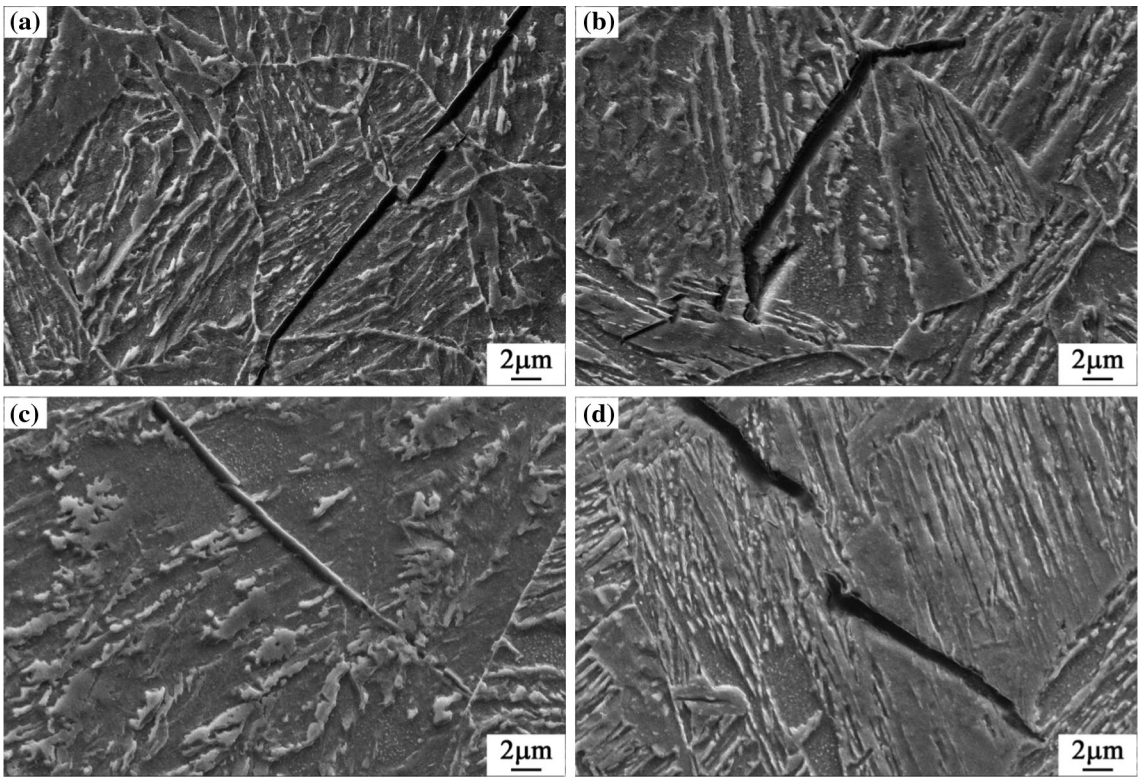

Fig. 15 Packet-sized cracks retained in the specimens austenitized at (a) 950 °C, (b) 1100 °C, (c) and (d) 1250 °C, all failed at − 196 °C

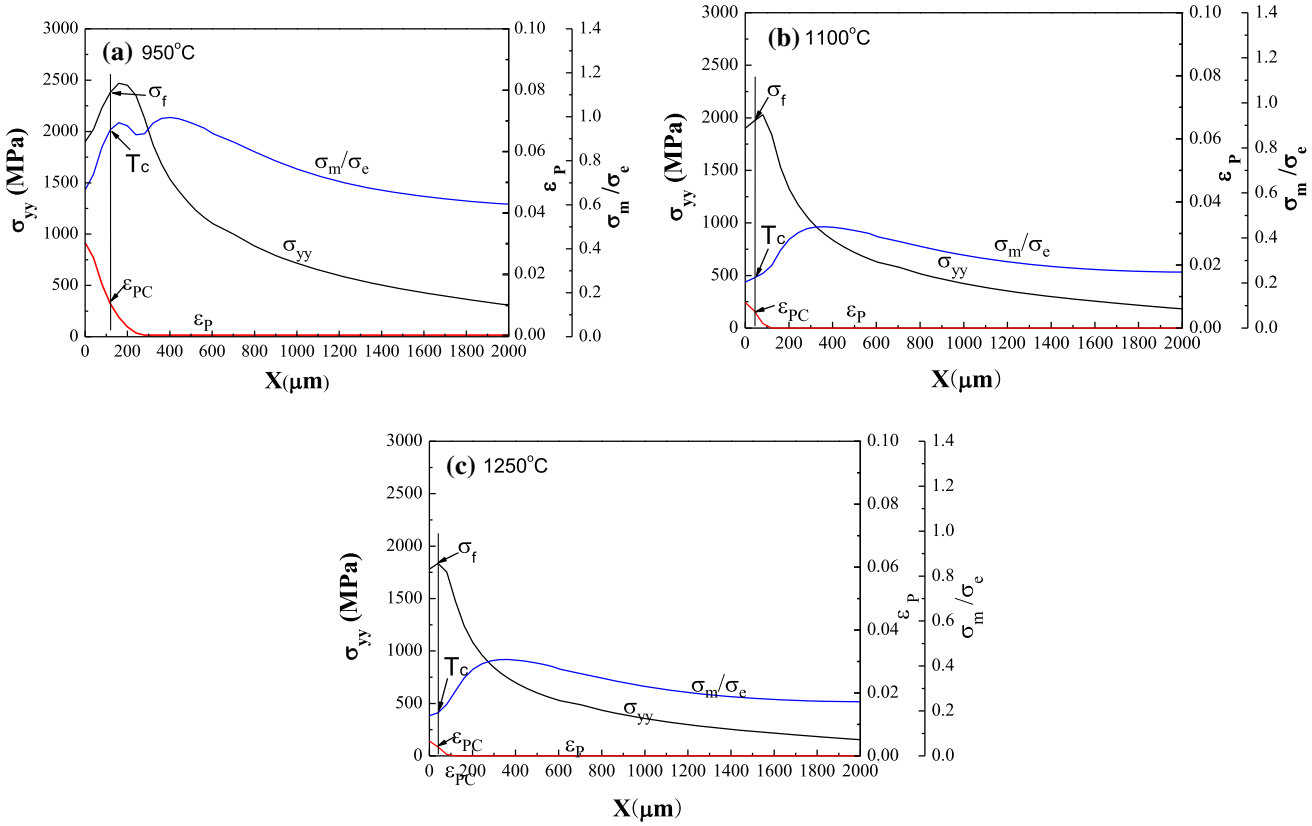

Fig. 16 Stress, strain, and stress triaxiality distributions ahead of the notch at fracture stress at − 196 °C for the specimen austenitized at (a) 950 °C, (b) 1100 °C, and (c) 1250 °C

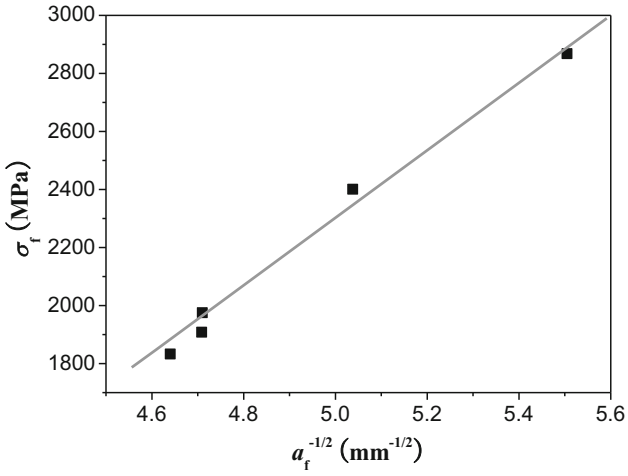

Fig. 17 Change in σ_f as a function of a_f

5. Conclusion

The present work obtained DBTTs, P_y, P_f, σ_{dy}, of the specimens by using the CVN testing. The values of σ_f have been determined by means of FEM and the measured X_f. The microstructural factors, prior austenite size, packet size, and the fraction of HAGBs, have also been experimentally measured. The bridge connecting the DBTT, σ_f, and the key microstructural factors has therefore been established, and the following conclusions were drawn.

1. The resultant microstructures at room temperature of the continuous cooling transformation (CCT) are evolved from mixture of lath bainite + granular bainite + lath martensite, to lath bainite + lath martensite as the isothermal austenitizing temperature changes being 950 °C, and to 1050-1250 °C. The rise of austenitizing temperature results in the largest austenite grains coarsened, being 42.3, 67.3, 106.20, and 323.9 μm, and correspondingly makes the packets larger, being 39.5, 42.0, 53.8, and 95.7 μm for the austenitizing temperatures at 950, 1050, 1100, and 1250 °C.
2. The ductile-to-brittle transition temperatures of the specimens austenitized at 950, 1100, and 1250 °C are − 80, − 67, and − 52 °C, respectively. The critical event for cleavage fracture is identified as the propagation of the packet-sized crack. The local cleavage fracture stress σ_f is determined, being 2401, 1975, and 1833 MPa, and the values of critical values of the stress intensification $Q_c = \sigma_f/\sigma_{dy}$ being 1.60, 1.29, and 1.26.
3. The packets' sizes play decisive role in increasing the resistance against brittle crack propagation. As a result, the size of cleavage facet area at the origin of the cleavage crack (a_f) increases as the size of the coarsest packets increases. The present work leads to a quantitative relationship between σ_f and a_f in the lathy microstructures.

The σ_f for the specimen austenitized at 1050 °C is predicted, being 2314 MPa. This can thus explain the measured DBTT of the specimens being − 75 °C.

Acknowledgment

The authors acknowledge the financial support received from Jiansu Shagang Group Co., Ltd. Dr. Q. X. Feng is thanked for performing the thermomechanical tests.

References

1. J.W. Morris, Jr., Stronger, Tougher Steels, *Science*, 2008, **320**, p 1022–1023
2. T. Hanamura, F. Yin, and K. Nagai, Ductile–Brittle Transition Temperature of Ultrafine Ferrite Cementite Microstructure in a Low Carbon Steel Controlled by Effective Grain Size, *ISIJ Int.*, 2004, **44**, p 610–617
3. J.W. Morris, Jr., On the Ductile–Brittle Transition in Martensitic Steels, *ISIJ Int.*, 2011, **51**, p 1569–1575
4. S.Y. Shin, K.J. Woo, B. Hwang, S. Kim, and S. Lee, Fracture Toughness Analysis in Transition Temperature Region of Three American Petroleum Institute X70 and X80 Pipe Line Steels, *Metall. Mater. Trans. A*, 2009, **40A**, p 867–876
5. J.H. Chen and R. Cao, *Micromechanism of Cleavage Fracture of Metals. A Comprehensive Microphysical Model for Cleavage Cracking in Metals*, Elsevier, Oxford, 2014, ISBN 9780128007655
6. R. Cao, X.B. Zhang, Z. Wang, Y. Peng, W.S. Du, Z.L. Tian, and J.H. Chen, Investigation of Microstructural Features Determining the Toughness of 980 MPa Bainitic Weld Metal, *Metall. Mater. Trans. A*, 2014, **45A**, p 815–834
7. A. Di Schino and C. Guarnaschelli, Effect of Microstructure on Cleavage Resistance of High-strength Quenched and Tempered Steels, *Mater. Lett.*, 2009, **63**, p 1968–1972
8. N. Isasti, D. Jorge-Badiola, M.L. Taheri, and P. Uranga, Microstructural Features Controlling Mechanical Properties in Nb-Mo Microalloyed Steels. Part II: Impact Toughness, *Metall. Mater. Trans. A*, 2014, **45A**, p 4972–4982
9. S. Pallaspuro, A. Kaijalainen, S. Mehtonen, J. Kömi, Z. Zhang, and D. Porter, Effect of Microstructure on the Impact Toughness Transition Temperature of Direct-Quenched Steels, *Mater. Sci. Eng. A*, 2018, **A712**, p 671–680
10. J.P. Naylor, The Influence of the Lath Morphology on the Yield Stress and Transition Temperature of Martensitic–Bainitic Steels, *Metall. Trans. A*, 1979, **10A**, p 861–873
11. A.F. Gourgues, H.M. Flower, and T.C. Lindley, Electron Backscattering Diffraction Study of Acicular Ferrite, Bainite, and Martensite Steel Microstructures, *Mater. Sci. Technol.*, 2000, **16**, p 26–40
12. A. Lambert-Perlade, A.F. Gourgues, J. Besson, T. Sturel, and A. Pineau, Mechanisms and Modeling of Cleavage Fracture in Simulated Heat-Affected Zone Microstructures of a High-Strength Low Alloy Steel, *Metall. Mater. Trans. A*, 2004, **35A**, p 1039–1053
13. J.W. Morris, Jr., C.S. Lee, and Z. Guo, The Nature and Consequences of Coherent Transformations in Steel, *ISIJ Int.*, 2003, **43**, p 410–419
14. J.W. Morris, Jr., C. Kinney, K. Pytlewski, and Y. Adachi, Microstructure and Cleavage in Lath Martensitic Steels, *Sci. Technol. Adv. Mater.*, 2013, **14**, p 1–9
15. M. Tsuboi, A. Shibata, D. Terada, and N. Tsuji, Role of Different Kinds of Boundaries Against Cleavage Crack Propagation in Low-Temperature Embrittlement of Low-Carbon Martensitic Steel, *Metall. Mater. Trans. A*, 2017, **48A**, p 3261–3268
16. A. Ghosh, S. Das, and S. Chatterjee, Aging Behavior of a Cu-Bearing Ultrahigh Strength Steel, *Mater. Sci. Eng. A*, 2008, **486**, p 152–157
17. S.K. Dhua, D. Mukerjee, and D.S. Sarma, Effect of Cooling Rate on the As Quenched Microstructure and Mechanical Properties of HSLA-100 Steel Plates, *Metall. Mater. Trans. A*, 2003, **34A**, p 2493–2504
18. S.K. Dhua, D. Mukerjee, and D.S. Sarma, Influence of Tempering on the Microstructure and Mechanical Properties of HSLA-100 Steel Plates, *Metall. Mater. Trans. A*, 2001, **32A**, p 2259–2270
19. S.K. Dhua, A. Ray, and D.S. Sarma, Effect of Tempering Temperatures on the Mechanical Properties and Microstructures of HSLA-100 Type Copper-Bearing Steels, *Mater. Sci. Eng. A*, 2001, **A318**, p 197–210
20. P.K. Ray, R.I. Ganguly, and A.K. Panda, Optimization of Mechanical Properties of an HSLA-100 Steel Through Control of Heat Treatment Variables, *Mater. Sci. Eng. A*, 2003, **A346**, p 122–131
21. Y. You, X.M. Wang, and C.J. Shang, Influence of Austenitizing Temperature on the Microstructure and Impact Toughness of a High Strength Low Alloy HSLA100 Steel, *Acta Metall. Sin.*, 2012, **48**, p 1290–1298
22. D.S. Liu, B.G. Cheng, and Y.Y. Cheng, Strengthening and Toughening of a Heavy Plate Steel for Shipbuilding with Yield Strength of Approximately 690 MPa, *Metall. Mater. Trans. A*, 2013, **44A**, p 440–455
23. B.G. Cheng, M. Luo, and D.S. Liu, High Strength, Low Carbon, Cu-Containing Steel Plates with Tailored Microstructure and Low Yield Ratio', *Ironmak. Steelmak.*, 2015, **42**, p 608–617
24. D.S. Liu, B.G. Cheng, and Y.Y. Cheng, Fine Microstructure and Toughness of Low Carbon Copper Containing Ultrahigh Strength NV F690 Heavy Steel Plate, *Acta Metall. Sin.*, 2012, **48**, p 334–342
25. G. Spanos, R.W. Fonda, R.A. Vandermeer, and A. Matuszeski, Microstructural Changes in HSLA-100 Steel Thermally Cycled to Simulate the Heat-Affected-Zone during Welding, *Metall. Mater. Trans. A*, 1995, **26A**, p 3277–3293
26. M. Shome and O.N. Mohanty, Continuous Cooling Transformation Diagrams Applicable to the Heat-Affected Zone of HSLA-80 and HSLA-100 Steels, *Metall. Mater. Trans. A*, 2006, **37A**, p 2159–2169
27. D. Chae, C.J. Young, D.M. Goto, and D.A. Kos, Failure Behavior of Heat-Affected Zones Within HSLA-100 and HY-100 Steel Weldments, *Metall. Mater. Trans. A*, 2001, **32A**, p 2229–2237
28. S.K. Dhua, D. Mukerjee, and D.S. Sarma, Weldability and Microstructural Aspects of Shielded Metal Arc Welded HSLA-100 Steel Plates, *ISIJ Int.*, 2002, **42**(3), p 290–298
29. K. Banerjee and U.K. Chatterjee, Effect of Microstructure on Hydrogen Embrittlement of Weld-Simulated HSLA-80 and HSLA-100 Steels, *Metall. Mater. Trans. A*, 2003, **34A**, p 1297–1309
30. K. Banerjee, M. Militzer, M. Perez, and X. Wang, Nonisothermal Austenite Grain Growth Kinetics in a Microalloyed X80 Linepipe Steel, *Metall. Mater. Trans. A*, 2010, **41A**, p 3161–3172
31. R. Cao, J. Li, D.S. Liu, J.Y. Ma, and J.H. Chen, Micromechanism of Decrease of Impact Toughness in Coarse-Grain Heat-Affected Zone of HSLA Steel with the Increasing Weld Heat Input, *Metall. Mater. Trans. A*, 2015, **46A**, p 2999–3014
32. D.S. Liu, M. Luo, B.G. Cheng, R. Cao, and J.H. Chen, Microstructural Evolution and Ductile-to-Brittle Transition in a Low Carbon MnCrMoNiCu Heavy Plate Steel, *Metall. Mater. Trans. A*, 2018. https://doi.org/10.1007/s11661-018-4823-9
33. D.S. Liu, Q.L. Li, and T. Emi, Microstructure and Mechanical Properties in Hot Rolled Extra-High-Yield-Strength Steel Plates for Offshore Structure and Shipbuilding, *Metall. Mater. Trans. A*, 2011, **42A**(5), p 1349–1361
34. W.L. Server, General Yielding of Charpy V-Notch and Precracked Charpy Specimens, *J. Eng. Mater. Technol.*, 1978, **100**, p 183–188
35. E.I. Galindo-Nava and P.E.J. Rivera-Diaz-del-Castillo, Model for the Microstructure Behaviour and Strength Evolution in Lath Martensite, *Acta Mater.*, 2015, **98**, p 81–93
36. S.Y. Sung, S.S. Sohn, S.Y. Shin, K.S. Oh, and S. Lee, Effects of Oxides on Tensile and Charpy Impact Properties and Fracture Toughness in Heat Affected Zones of Oxide-Containing API, X80 Linepipe Steels, *Metall. Mater. Trans. A*, 2014, **45A**, p 3036–3050
37. M. Shome, D.S. Sarma, O.P. Gupta, and O.N. Mohanty, Precipitate Dissolution and Grain Growth in the Heat Affected Zone of HSLA-100 Steel, *ISIJ Int.*, 2003, **43**, p 1431–1437